

The role of fiber gauge lengths in elastic FWI of data from coiled DAS fibers

Matt Eaid, Scott Keating and Kris Innanen

ABSTRACT

Distributed acoustic sensing is an important technology that offers distinct benefits for reservoir monitoring. The increased access they provide to borehole acquisition geometries, has the potential to supply transmission data crucial to successful applications of full waveform inversion on land data. The properties of the fiber such as its geometric shape, and its gauge length, especially in relation to the geometry, are expected to have implications for parameter resolution in FWI. In this paper we explore the role of the fiber gauge length in FWI, by examining (1) how it affects a given fiber's sensitivity to each component of the strain field, and (2) how the relative sensitivity to these strain components affects parameter resolution. This is explored through numerical simulations on a simple model on both clean and noisy data, as well as a more complex, and geologically reasonable model.

INTRODUCTION

Full waveform inversion (FWI) is a powerful tool for estimating the spatial distribution of subsurface properties (Tarantola, 1984, 1986). Elastic FWI, proposed by Tarantola (1986), assumes isotropic-elastic wave physics, and focuses on estimating the spatial distribution of three elastic parameters, typically P-wave velocity (v_p), S-wave velocity (v_s), and density (ρ) to characterize the medium. The successful application of FWI faces the two major challenges of cycle skipping, and cross-talk when applied to land data. Cycle skipping occurs when the observed and modeled data are out of phase by more than one half cycle, causing adjacent cycles to align during minimization, leading to erroneous updating of the model. Its occurrence is a result of the choice of objective function and the data quality as a function. While mitigation strategies focusing on the choice of objective function have been developed (van Leeuwen and Mulder, 2010; Luo and Sava, 2011; Warner and Guasch, 2016; Metivier et al., 2018), the single best method for combating cycle skipping is to acquire the long-wavelength data that prevents the matching of adjacent cycles. Cross-talk is also a function of the acquisition geometry, and occurs when the perturbation of two subsurface properties produces similar perturbations in the wavefield over the acquisition aperture. When this occurs, changes in the wavefield could reasonably be caused by a perturbation in either property, and FWI can erroneously update the incorrect property. From this discussion, it is evident that the acquisition geometries afforded by our sensor technology are paramount for land applications of elastic FWI.

The prevalent technology for recording the wavefields required for elastic FWI, are 3C geophones. This is due in large part to their ability to economically provide multiple components of high signal-to-noise ratio (SNR) data. However, geophones come with a major drawback. The size of geophones limits their access to the borehole geometries crucial for providing transmission type data. Geophones often affect production processes in boreholes, requiring dedicated monitoring wells, or production shut-in for their deployment. The expense of horizontal wells, means that geophones are rarely deployed in them, as

dedicated monitor wells, and shut-in become uneconomical. The transmission data that can be acquired with sensors in borehole geometries provides crucial long-wavelength information about the subsurface than mitigate cycle-skipping. Additionally, cross-talk can be strongly mitigated when we have access to large aperture recording provided by a combination of surface and borehole recording (Pan et al., 2018).

A relatively new technology that provides enhanced access to borehole geometries is distributed acoustic sensing (DAS). Using non-invasive optical fibers for sensing seismic strain, DAS can economically deployed in boreholes without requiring dedicated monitoring wells, or well shut-in. However, due to the rigidity of the optical fibers employed in DAS, they are only sensitive to those normal components of strain along the tangential component of the fiber (Kuvshinov, 2015). Shaping DAS fibers, into e.g. a helix, alters the tangents sampled by the fiber which has important implications on the parameter resolution that can be obtained through FWI (Eaid et al., 2020). It is also important to note that DAS sensors are not point sensors. To improve signal-to-noise, the strain measurements are averaged over a spatial length of fiber on the order of ten-meters, known as the gauge length (Dou et al., 2017). This limits the benefit of shaping fibers by averaging away some of the enhanced sensitivity they supply. In fact, most commonly deployed fiber geometries fall into a symmetry class of fibers insensitive to shear strains (Eaid et al., 2020). However, Farhadiroushan et al. (2016) indicate that small gauge lengths on the order of 5cm appear to be on the horizon. In this paper we are interested in exploring how gauge lengths smaller than the distance advanced by a helical wind of fiber, which unlocks access to the shear strains, influences parameter resolution in FWI. This will be explored using a number of simple models and numerical simulations.

SIMULATION OF DAS DATA

Developing an inversion framework for DAS data requires a general methodology for simulating the data supplied by DAS fibers. This requires two main components, a method of simulating isotropic-elastic wavefield propagation, and a geometric model for the fiber that allows for projection of this elastic wavefield onto the tangent of the fiber. In this paper we consider 2D frequency domain isotropic-elastic wave propagator that involves medium perturbations in depth and the inline coordinate, but not the cross-line (y) direction. The fiber, is a 3D object, but is embedded in a medium with no wavefield or medium variations in the y-direction, allowing us to consider only its x-z properties.

Elastic wavefield simulation

Following from Pratt (1990), the 2D displacement wavefield is computed through solution to the coupled system of equations:

$$\omega^2 \rho u_x + \frac{\partial}{\partial x} \left[\lambda \left(\frac{\partial u_x}{\partial x} + \frac{\partial u_z}{\partial z} \right) + 2\mu \frac{\partial u_x}{\partial x} \right] + \frac{\partial}{\partial z} \left[\mu \left(\frac{\partial u_z}{\partial x} + \frac{\partial u_x}{\partial z} \right) \right] + s_x = 0 \quad (1a)$$

$$\omega^2 \rho u_z + \frac{\partial}{\partial z} \left[\lambda \left(\frac{\partial u_x}{\partial x} + \frac{\partial u_z}{\partial z} \right) + 2\mu \frac{\partial u_z}{\partial z} \right] + \frac{\partial}{\partial x} \left[\mu \left(\frac{\partial u_z}{\partial x} + \frac{\partial u_x}{\partial z} \right) \right] + s_z = 0 \quad (1b)$$

where $u_x = u_x(x, z, \omega)$, and $u_z = u_z(x, z, \omega)$ are the x - and z -components of the frequency domain particle displacement; $\lambda = \lambda(x, z)$ and $\mu = \mu(x, z)$ are the Lamé parameters; $\rho = \rho(x, z)$ is the density; and s_x and s_z are x and z -components of the frequency domain source function. Solving equations (1a) and (1b) provides the x and z -components of the frequency domain particle displacements. The associated components of the strain field in the x - z plane, solved on a grid staggered from the displacement grid are,

$$\epsilon_{xx} = \frac{1}{2\Delta x} [u_x(x_{n+1}, z_{n+1}) - u_x(x_n, z_{n+1}) + u_x(x_{n+1}, z_n) - u_x(x_n, z_n)] \quad (2a)$$

$$\begin{aligned} \epsilon_{xz} = & \frac{1}{4\Delta x} [u_z(x_{n+1}, z_{n+1}) - u_z(x_n, z_{n+1}) + u_z(x_{n+1}, z_n) - u_z(x_n, z_n)] \\ & + \frac{1}{4\Delta z} [u_x(x_{n+1}, z_{n+1}) - u_x(x_{n+1}, z_n) + u_x(x_n, z_{n+1}) - u_x(x_n, z_n)] \end{aligned} \quad (2b)$$

$$\epsilon_{zz} = \frac{1}{2\Delta z} [u_z(x_{n+1}, z_{n+1}) - u_z(x_{n+1}, z_n) + u_z(x_n, z_{n+1}) - u_z(x_n, z_n)]. \quad (2c)$$

Fiber response

Generation of the local fiber response requires projection of the strain field in the (x, y, z) coordinate system described by equations (2a)-(2c), into a Frenet-Serret coordinate system in the tangent $\hat{\mathbf{t}}(s)$, normal $\hat{\mathbf{n}}(s) = \mathbf{n}(s)/|\mathbf{n}(s)|$ where $\mathbf{n}(s) = d\hat{\mathbf{t}}(s)/ds$ and the bi-normal $\hat{\mathbf{b}}(s) = \hat{\mathbf{t}}(s) \times \hat{\mathbf{n}}(s)$ along the arc-length s . At time t , and arc-length s along the fiber, the strain in this Frenet-Serret coordinate system,

$$\epsilon_{tnb} = \mathbf{P}(s)\epsilon_{xyz}\mathbf{P}(s)^T \quad (3)$$

where $\mathbf{P}(s)$ is a rotation operator transforming between the two systems, defined by,

$$\mathbf{P}(s) = \begin{bmatrix} \hat{\mathbf{t}}(s) \cdot \hat{\mathbf{x}} & \hat{\mathbf{t}}(s) \cdot \hat{\mathbf{y}} & \hat{\mathbf{t}}(s) \cdot \hat{\mathbf{z}} \\ \hat{\mathbf{n}}(s) \cdot \hat{\mathbf{x}} & \hat{\mathbf{n}}(s) \cdot \hat{\mathbf{y}} & \hat{\mathbf{n}}(s) \cdot \hat{\mathbf{z}} \\ \hat{\mathbf{b}}(s) \cdot \hat{\mathbf{x}} & \hat{\mathbf{b}}(s) \cdot \hat{\mathbf{y}} & \hat{\mathbf{b}}(s) \cdot \hat{\mathbf{z}} \end{bmatrix}. \quad (4)$$

Due to the rigidity of the glass in DAS fibers, they are sensitive only to the normal component of tangential strain ϵ_{tt} . The localized DAS fiber response, computed by solving equation (3) and extracting the ϵ_{tt} component is,

$$\epsilon_{tt} = (\hat{\mathbf{t}} \cdot \hat{\mathbf{x}})^2 \epsilon_{xx} + 2(\hat{\mathbf{t}} \cdot \hat{\mathbf{x}})(\hat{\mathbf{t}} \cdot \hat{\mathbf{y}}) \epsilon_{xy} + 2(\hat{\mathbf{t}} \cdot \hat{\mathbf{x}})(\hat{\mathbf{t}} \cdot \hat{\mathbf{z}}) \epsilon_{xz} + (\hat{\mathbf{t}} \cdot \hat{\mathbf{y}})^2 \epsilon_{yy} + 2(\hat{\mathbf{t}} \cdot \hat{\mathbf{y}})(\hat{\mathbf{t}} \cdot \hat{\mathbf{z}}) \epsilon_{yz} + (\hat{\mathbf{t}} \cdot \hat{\mathbf{z}})^2 \epsilon_{zz}. \quad (5)$$

Equation (5) represents the strain sensed by the DAS fiber, if it were to measure localized point measurements, however, with current technology this leads to insufficient signal-to-noise. In practice, the interrogator unit that processes light backscattered from the fiber, combines interference patterns from two scattering centers to infer strain. This interrogator contains an unbalanced Mach-Zehnder interferometer that delays the signal from the second scattering center, combining the interference patterns from two separated portions of fiber, where the separation distance is the gauge length. All of the strain between the two scattering centers contributes to the displacement of the second scattering center, and for this reason, DAS supplies an average of the strain over the gauge length. The DAS datum, averaged over gauge length L , for a fixed time t is,

$$d(s) = \int_{-L/2}^{L/2} W(s - s', L) \epsilon_{tt}(s') ds' \quad (6)$$

where,

$$W(s, L) = \begin{cases} 1/L, & -L/2 < s < L/2 \\ 0, & \text{otherwise} \end{cases} . \quad (7)$$

Assuming the strain is approximately constant over the gauge length L , equation (6) can be written as,

$$\begin{aligned} d(s) = & \epsilon_{xx} \int_{-L/2}^{L/2} t_x(s')^2 ds' + 2\epsilon_{xy} \int_{-L/2}^{L/2} t_x(s') t_y(s') ds' + 2\epsilon_{xz} \int_{-L/2}^{L/2} t_x(s') t_z(s') ds' \\ & + \epsilon_{yy} \int_{-L/2}^{L/2} t_y(s')^2 ds' + 2\epsilon_{yz} \int_{-L/2}^{L/2} t_y(s') t_z(s') ds' + \epsilon_{zz} \int_{-L/2}^{L/2} t_z(s')^2 ds' \end{aligned} \quad (8)$$

Sensitivity of DAS fibers

Consider a fiber of arbitrary shape embedded in a generalized 3D elastic medium, and let the fiber be parameterized by the direction of its core $\hat{\mathbf{c}}$ and the two components of a plane normal to this core $\hat{\mathbf{p}}_1$ and $\hat{\mathbf{p}}_2$. This fiber has the datum,

$$\begin{aligned} d(s) = & \epsilon_{cc} \int_{-L/2}^{L/2} t_c(s')^2 ds' + 2\epsilon_{cp_1} \int_{-L/2}^{L/2} t_c(s') t_{p_1}(s') ds' + 2\epsilon_{cp_2} \int_{-L/2}^{L/2} t_c(s') t_{p_2}(s') ds' \\ & + \epsilon_{p_1 p_1} \int_{-L/2}^{L/2} t_{p_1}(s')^2 ds' + 2\epsilon_{p_1 p_2} \int_{-L/2}^{L/2} t_{p_1}(s') t_{p_2}(s') ds' + \epsilon_{p_2 p_2} \int_{-L/2}^{L/2} t_{p_2}(s')^2 ds' . \end{aligned} \quad (9)$$

Now consider a symmetry class of fibers, such that within one wind of this fiber, for every point k there exists another point $k + \delta_k$, such that the direction of the core is preserved,

but the directions of both p_1 and p_2 are reversed as plotted in Figure 1. This definition of symmetry was defined by Eaid et al. (2020), and includes some of the commonly proposed geometries, including straight fibers, helical fibers, and chirped helical fiber (Ning and Sava, 2018). If the gauge length contains an integer number of winds, or sufficiency many winds such that a small amount of fiber outside the gauge length contributes negligibly, then the shear strain components in equation (9) disappear, showing this symmetry class of fibers is insensitive to shear strain.

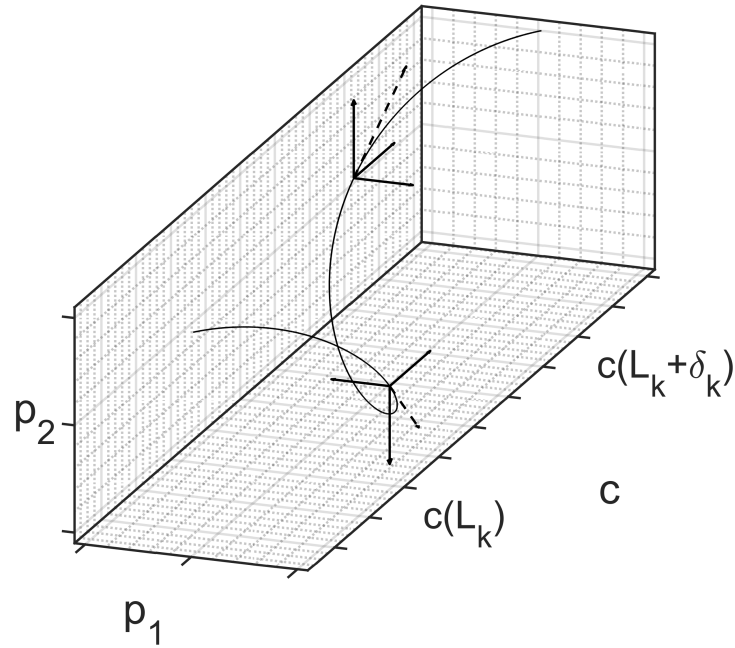


FIG. 1. Example of a section of symmetric fiber, showing change in sign of $\hat{\mathbf{t}}(s) \cdot \hat{\mathbf{p}}(s)$ and preservation of the sign of $\hat{\mathbf{t}}(s) \cdot \hat{\mathbf{c}}(s)$ from L_k to $L_k + \delta_k$. The thin line represents a section of symmetric fiber, the dashed lines the tangent to the fiber, and the thick lines the components of the tangent $\hat{\mathbf{t}}(s) \cdot \hat{\mathbf{c}}$, $\hat{\mathbf{t}}(s) \cdot \hat{\mathbf{p}}_1$, and $\hat{\mathbf{t}}(s) \cdot \hat{\mathbf{p}}_2$.

This means that the symmetry class of fibers, representing the majority of deployed fibers, are insensitive to a large, and potentially important to FWI, portion of the wave-field. We are left with two options, design some complex fiber geometry that violates this definition of symmetry (Eaid et al., 2020), or assume gauge lengths much shorter than the distance advanced by the fiber, such that the definition of symmetry is violated over the gauge length. Helical fiber geometries have been deployed with radii of 2.54cm with winds of approximately 30° . The distance advanced by a fiber of this geometry is,

$$h = \frac{2\pi(2.54\text{cm})}{\tan(30^\circ)} \approx 27.64\text{cm}. \quad (10)$$

Farhadiroushan et al. (2016) develop a DAS system with the potential for 5cm gauge lengths. Thus it would appear that gauge lengths smaller than the distance h advanced by one period of typical fiber geometries (equation (10)), are plausible.

Figure 2a plots a segment of a helical fiber in a horizontal well, with a lead angle of 19.5° . The sensitivities of this fiber to ϵ_{xx} , ϵ_{xz} , and ϵ_{zz} are,

$$S_{xx} = \int_{-L/2}^{L/2} t_x(s')^2 ds' \quad S_{xz} = 2 \int_{-L/2}^{L/2} t_x(s')t_z(s') ds' \quad S_{zz} = \int_{-L/2}^{L/2} t_z(s')^2 ds'. \quad (11)$$

Figure 2a shows a fiber that advances 24cm in one wind in black, and a length interrogated by this fiber in green. Figures 2b-2d plot the sensitivities for this fiber with a gauge length much longer than the distance of the fiber (72cm in blue), a gauge length much shorter (8cm in red), and a gauge length of zero giving the point-wise sensitivity (black).

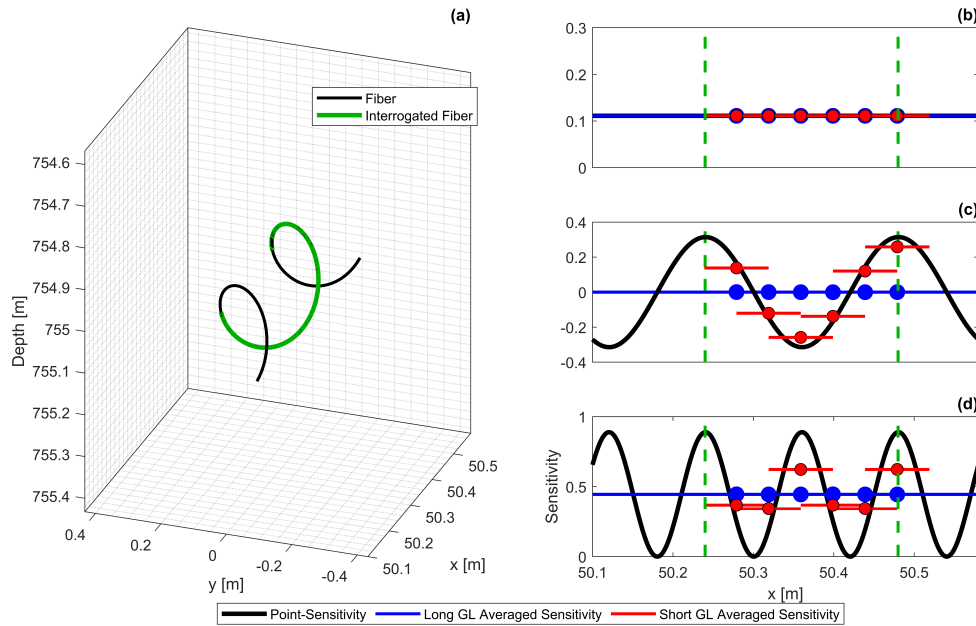


FIG. 2. (a) A section of 19.5° helical fiber (black) and an interrogated wind of this fiber (green). (b) Sensitivity of the fiber in (a) to ϵ_{xx} , (c) sensitivity of the fiber in (a) to ϵ_{xz} , and (d) sensitivity of the fiber in (a) to ϵ_{zz} . The black line is the point-wise sensitivity, the blue points are the long gauge length averaged sensitivity, and the red points are the short gauge length averaged sensitivity. The blue and red lines indicate the gauge length over which the sensitivity is averaged. The green dashed lines represent the wind of interrogated fiber in (a).

Figure 3 explains why short gauge length fibers have increased sensitivity. When the gauge length is much longer than the wind of the fiber, the projections $(\hat{\mathbf{t}}(s') \cdot \hat{\mathbf{x}})^2$, and $(\hat{\mathbf{t}}(s') \cdot \hat{\mathbf{z}})^2$ are constant and equal to their mean value over the wind, furthermore $2(\hat{\mathbf{t}}(s') \cdot \hat{\mathbf{x}}\hat{\mathbf{t}}(s') \cdot \hat{\mathbf{z}}) = 0$. Figure 3a shows a single wind of helical fiber (black line). When the gauge length, L , is much shorter than the fiber wind, the segment of fiber can be broken into sections of length L over which the sensitivities can be averaged. Figure 3a plots these sections with the red, blue, and green segments, and their associated tangents. Each of these sections samples a different subset of tangents, and therefore sensitivity. Figure 3b-3d shows the sensitivities explored by each segment, and gauge length averaged sensitivity by the colored dots. Clearly, each segment has a different sensitivity to the wavefield,

highlighting that short gauge length fibers have enhanced sensitivity to a larger portion of the wavefield.

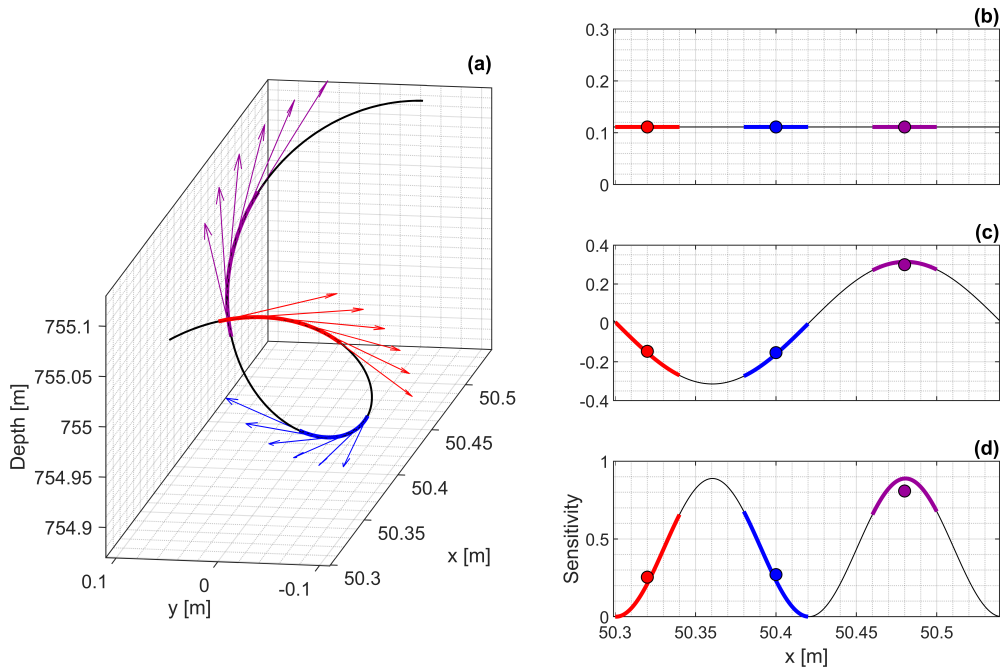


FIG. 3. (a) One wind of helical fiber (black) and three segments of length equal to the gauge length and their tangents (red, green, and blue). Sensitivity of these segments to (b) ϵ_{xx} , (c) ϵ_{xz} , and (d) ϵ_{zz} . The colored lines show the point-wise sensitivity of each segment, and the colored dots the gauge length averaged sensitivity.

Figures 2b-2d highlight that for a fiber oriented in the x-direction, with long gauge lengths relative to the distance advanced by the fiber, have reduced sensitivity to ϵ_{zz} , relative to a fiber with a short gauge length. Furthermore, the long gauge length fiber is fully insensitive to shear strain ϵ_{xz} , while the short gauge length fiber has nearly complete sensitivity to this component. We are interested in how gauge lengths much shorter than distance advanced by one wind of the fiber, providing access to a larger portion of the wavefield, in the form of shear strains, affects parameter resolution in FWI.

FWI OF DAS DATA

The objective function in conventional least-square FWI, measuring the L_2 norm of the difference between observed data and modeled data is,

$$\phi = \frac{1}{2} \|\mathbf{R}\mathbf{u} - \mathbf{d}\|_2^2 \quad (12)$$

where \mathbf{R} is a matrix transforming the modeled wavefield \mathbf{u} into quantities directly comparable with the observed data \mathbf{d} . Equation 12 can be written as a constrained optimization problem,

$$\min_{\mathbf{m}} = \frac{1}{2} \|\mathbf{R}\mathbf{u} - \mathbf{d}\|_2^2 \quad \text{subject to} \quad \mathbf{S}\mathbf{u} = \mathbf{f} \quad (13)$$

where \mathbf{m} is a vector of model parameters, \mathbf{S} is a wave equation operator, and \mathbf{f} is the source function. Using Lagrange multipliers, and the adjoint state method (Metivier et al., 2013), the gradient of equation (12) is,

$$\mathbf{g} = \frac{\partial \phi}{\partial \mathbf{m}} = \left\langle \frac{\partial \mathbf{S}}{\partial \mathbf{m}} \mathbf{u}, \lambda \right\rangle \quad (14)$$

where, $\langle \dots \rangle$ represents the inner product, and λ is the adjoint wavefield computed through solving the adjoint wavefield problem,

$$\mathbf{S}^\dagger \lambda = \mathbf{R}^\dagger (\mathbf{R}\mathbf{u} - \mathbf{d}). \quad (15)$$

The FWI update direction, $\Delta \mathbf{m}$, in this paper is given by approximate, truncated Gauss-Newton solutions to the problem,

$$\mathbf{H} \Delta \mathbf{m} = -\mathbf{g} \quad (16)$$

\mathbf{H} is the Hessian matrix.

Inclusion of DAS in FWI

The above discussion on the development of FWI equations for our problem typically assumes multi-component geophone data for \mathbf{d} , and simulated displacement components for \mathbf{u} , allowing us to perform FWI of geophone data. However, it is important to note that no assumptions are made about the matrix \mathbf{R} . This matrix has the responsibility of transforming the wavefield \mathbf{u} into a form that is comparable to \mathbf{d} . If we assume that \mathbf{d} consists of measurements made with a DAS fiber or arbitrary geometry, then the development of a matrix \mathbf{R} that simulates DAS data according to the above discussion, will allow for inclusion of DAS data in FWI. Following from the previous discussion, the matrix \mathbf{R} for DAS data, must

1. Compute the strain tensor at the locations of the DAS receivers using equations (2a)-(2c).
2. Average the sensitivities of the fiber over the gauge length and compute the fiber response using equation (8).

We are interested in understanding how the gauge length in relation to the fiber geometry, and the extra wavefield components sub-period gauge lengths provide access to, affect parameter resolution in FWI.

NUMERICAL RESULTS

Inversion of DAS data from a coiled-fiber with varying gauge lengths: Simple model

To investigate the role the gauge length of coiled fibers, especially in relation to the fiber geometry, has on the quality of parameter estimates from FWI, we will invert data from a helical DAS fiber with varying gauge length. Figure 4a-4c plots the true models in density, P-wave velocity (V_p), and S-wave velocity (V_s). Starting models are equal to the background values of $\rho = 1400 \text{ kg/m}^3$, $V_p = 3000 \text{ m/s}$, and $V_s = 1800 \text{ m/s}$.

Data were generated from these models using 33 explosive sources, spaced 30 meters apart at a depth of 30 meters. The data were recorded with a four fibers in a horizontal well oriented in the x-direction at a depth of 750 meters. Each fiber had a lead angle of 19.5° that results in an advance of 24 cm per turn. The fiber fibers have gauge lengths of 10.08 meters, 24cm, 18cm, and 3cm. A dataset was also recorded with geophones spaced at 10 meters, and at the same 750 meter depth as the fiber. These data were inverted over 10 frequency bands with a multi-scale (Bunks, 1995), truncated Gauss-Newton optimization with the Hessian approximated by 25 iterations of L-BGFS. Each iteration consists of five evenly spaced frequencies, with the minimum frequency set to 1 Hz in each iteration, and the maximum frequency growing by 2Hz for each iteration from 2-20Hz. Figure 4d-4f plots the inversion for data from the fiber with a 10.08 meter gauge length, Figure 4g-4i for the 24cm gauge length, Figure 4j-4l for the 18cm gauge length, and Figure 4m-4o for the 3cm gauge length. Figure 4p-4r plots the inversion results using the geophone data. The relative least square error (RLSE) per frequency band is plotted in Figure 5 for all four fibers, and the geophone inversion results.

Figures 4 and 5 highlight the important effect of sub-period gauge lengths. Figures 4d-4f and 4g-4i plot the inversion results for density, V_p , and V_s for two fibers with $L = 42h$ and $L = h$ where L is the gauge length, and h is the distance advanced by one helix wind. Both fibers provide identical inversion results, which is a direct result of the fact that both provide the same wavefield sensitivity due to their super-period gauge lengths. Gauge lengths longer than the helix period average away a significant portion of the enhanced sensitivity provided by the coiling of the fiber, resulting a marked degradation in the inversion quality. Gauge lengths smaller than the fiber period, provide access to better sampling of more tangent directions, and enhanced sensitivity as suggest by Figure 2 and 3. The sensitivity to shear strains, and enhanced sensitivity to ϵ_{zz} in our examples results in marked improvements in the inversion results, especially for V_s . Figures 4j-4l and 4m-4o plot inversion results for $L = 3h/4$ and $L = h/8$. Comparison of these inversion results to those for geophones in Figures 4p-4r, suggests that as the gauge length decreases and DAS approaches a point sensor, inversion results comparable to those obtained with true point sensors like geophones are plausible. Figures 5b and 5c, plotting the relative least squared error for V_p and V_s , shows that a marked improvement in the inversion is evident at point where the gauge length drops below the fiber period, and that as the gauge length approaches zero, DAS inversion results approach the quality of those supplied by a point sensor.

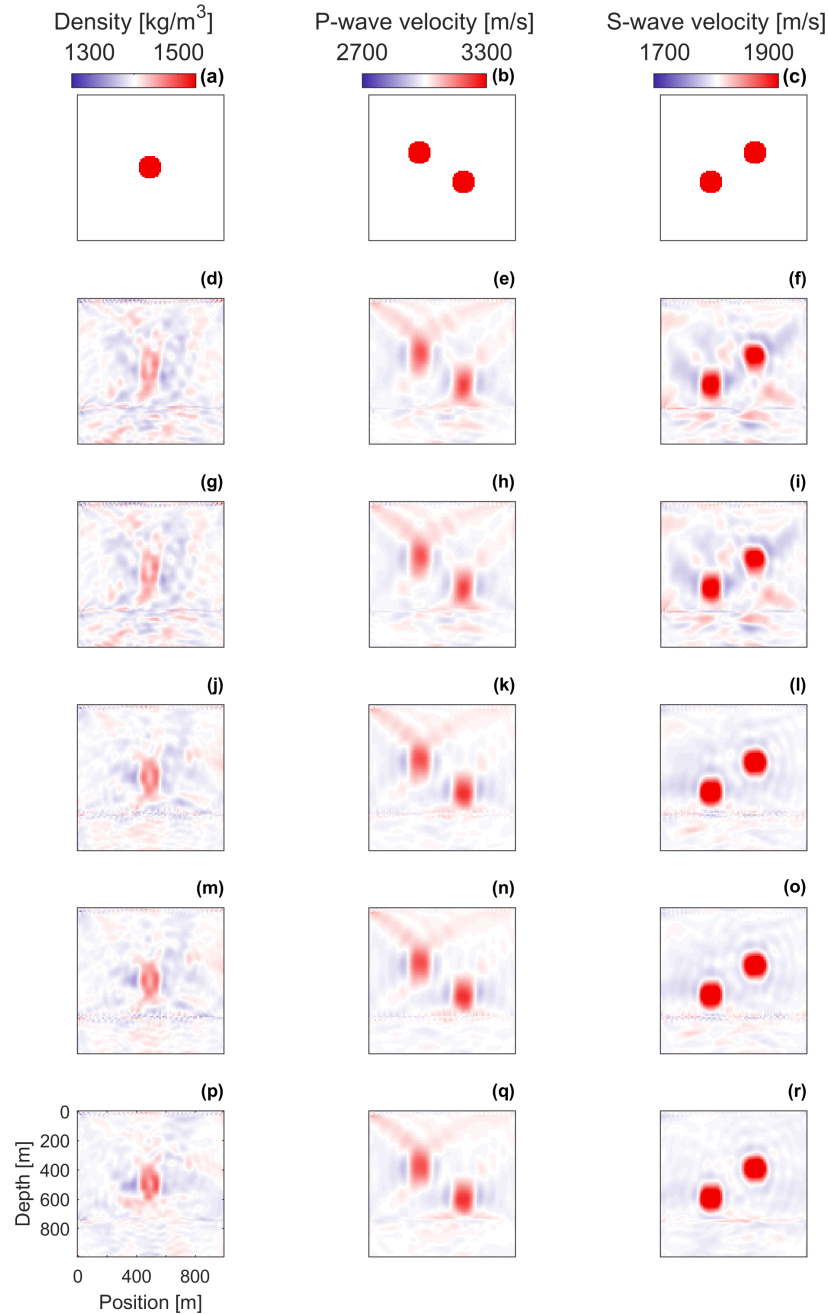


FIG. 4. (a)-(c) True models for density, P-wave velocity, and S-wave velocity. Inversions for density (column 1), P-wave velocity (column 2), and S-wave velocity (column 3), (d)-(f) for a gauge length of 10.08 m, (g)-(i) for a gauge length of 24 cm, (j)-(l) for a gauge length of 18 cm, (m)-(o) for a gauge length of 3 cm, and (p)-(r) for geophones.

CONCLUSIONS

Distributed acoustic sensing is becoming a prevalent technology for reservoir monitoring due to the ease with which it can be deployed in borehole geometries, without the need

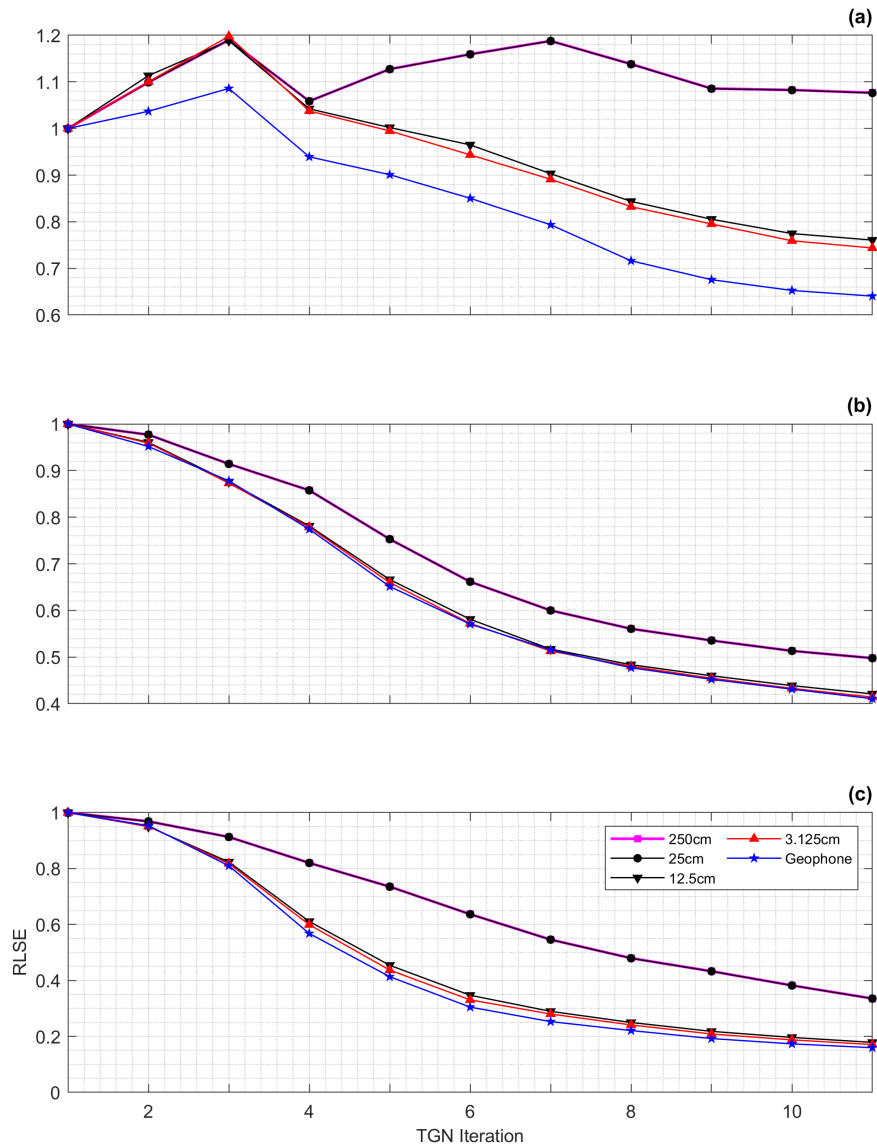


FIG. 5. (a) Relative least squares error per TGN iteration for the density inversions, (b) V_p inversion, and (c) V_s inversion. The magenta line represents the RLSE for the 10.08 meter gauge length, the black lines for intermediate lengths (24cm and 18cm), the red line for the 3cm gauge length, the blue represents the RLSE for the geophone inversions.

for dedicated monitoring wells. To realize the full potential of the data they can supply, it is important to develop a methodology for their inclusion in FWI as well as appraisal tools for understanding how the fiber properties affect inversion resolution. We briefly review the development of Eaid et al. (2020) for the inclusion of DAS data in FWI, in which the effect of geometry on parameter resolution was explored. In this paper, we explore the role of the gauge length in FWI of coiled DAS-fiber data. The results presented here suggest that DAS fibers can provide good inversion results, but to move DAS measurements closer

to those provide by true point sensors like geophones, gauge lengths have to fall below the periodicity of the fiber geometry. Encouragingly, with a realistic fiber geometry, we show that gauge lengths of 3cm produce inversion results comparable to those provided by geophones. Gauge lengths of this scale appear to be on the horizon (Farhadiroushan et al., 2016) and could make DAS a powerful reservoir monitoring technology.

ACKNOWLEDGMENTS

The authors would like to thank the sponsors of the CREWES project as well NSERC under the grants CRDPJ 461179-13 and CRDPJ 543578-19 for making this work possible through their financial support. Matt Eaid and Scott Keating were partially supported through scholarships from the SEG foundation.

REFERENCES

- Bunks, C., 1995, Multiscale seismic waveform inversion: *Geophysics*, **60**, No. 5.
- Dou, S., Lindsey, N., Wagner, A., Daley, T., Freifeld, B., Robertson, M., Peterson, J., Ulrich, C., Martin, E., and Ajo-Franklin, J., 2017, Distributed acoustic sensing for seismic monitoring of the near surface: A traffic-noise interferometry case study: *Scientific Reports*, **7**, No. 11620.
- Eaid, M. V., Keating, S. D., and Innanen, K. A., 2020, Multi-parameter seismic elastic full waveform inversion with combined geophone and shaped fiberoptic cable data: *GEOPHYSICS*, **0**, No. 6, 1–66.
- Farhadiroushan, M., Parker, T., and Shatalin, S., 2016, Method and apparatus for optical sensing: WO Patent App. PCT/GB2016/050.
- Kuvshinov, B. N., 2015, Interaction of helically wound fibre-optic cables with plane seismic waves: *Geophysical Prospecting*, **64**, No. 3.
- Luo, S., and Sava, P., 2011, A deconvolution-based objective function for wave-equation inversion: SEG Expanded Abstracts 81 International Meeting.
- Metivier, L., Allain, A., Brossier, R., Merigot, Q., Oudet, E., and Virieux, J., 2018, Optimal transport for mitigating cycle skipping in full-waveform inversion: A graph-space transform approach: *Geophysics*, **83**, No. 5, R515–R540.
- Metivier, L., Brossier, R., Virieux, J., and Operto, S., 2013, Full waveform inversion and the truncated newton method: *Siam J. Sci. Comput.*, **35**, B401–B437.
- Ning, I., and Sava, P., 2018, Multicomponent distributed acoustic sensing: Concept and theory: *Geophysics*, **83**, No. 2.
- Pan, W., Geng, Y., and Innanen, K. A., 2018, Interparameter trade-off quantification and reduction in isotropic-elastic full-waveform inversion: synthetic experiments and Hussar land data set application: *Geophysical Journal International*, **213**, No. 2, 1305–1333.
- Pratt, R., 1990, Frequency-domain elastic wave modeling by finite differences: A tool for crosshole seismic imaging: *Geophysics*, **55**, No. 5, 514–639.
- Tarantola, A., 1984, Inversion of seismic reflection data in the acoustic approximation: *Geophysics*, **49**.
- Tarantola, A., 1986, A strategy for nonlinear elastic inversion of seismic reflection data: *Geophysics*, **51**, 1893–1903.
- van Leeuwen, T., and Mulder, W., 2010, A correlation-based misfit criterion for wave-equation travel time tomography: *Geophysics Journal International*.
- Warner, M., and Guasch, L., 2016, Adaptive waveform inversion: theory: *Geophysics*, **74**, No. 6.